Optimization Methods and Software
Vol. 00, No. 00, Month 200x, 1–22

Optimizing Teardrop, an MRI Sampling Trajectory

Christopher Kumar Anand, Tingting Ren, Tamás Terlaky
Department of Computing and Software, McMaster University,
1280 Main St. W, ITB-202, Hamilton, ON, L8S 4K1, Canada
(3 September 2006)

Teardrop is an efficient sampling trajectory for acquiring Magnetic Resonance (MR) Imaging Data, especially balanced steady state free precession images. In this paper we present two models for optimizing such trajectories. These are the first models to incorporate motion-insensitivity constraints into a non-raster (also called spiral) sampling trajectory. The first model is nonlinear and very specific to Teardrop. The second model uses sequential second-order cone programming, and is generalisable to other trajectories in two and three dimensions. We present a weak convergence proof for the sequential method.

1 Introduction

Teardrop was introduced in [1] as a high-efficiency data collection strategy for balanced steady state free precession (bSSFP) imaging. It is efficient because it has a very high sampling duty cycle: collecting data 78 percent of the time in one example [1]. High-efficiency sampling has the potential of reducing scan times and capturing data faster for real-time imaging of rapid motion, *e.g.* cardiac imaging (see [2]). For a discussion of the mechanisms and merits of bSSFP imaging, see [3]. In this paper we present nonlinear and sequential second-order cone (SOC) models for the optimization of Teardrop control waveforms. These are the first models for general readout waveform design which incorporate velocity insensitivity. The sequential model is generalisable to other waveform design problems in Magnetic Resonance Imaging (MRI), and other trajectory problems which include global constraints, *e.g.* energy-minimizing exhaustive search patterns. We do not explore any applications outside MRI trajectories, but we present a proof of weak convergence which shows the approach is sound (*i.e.* produces improvements in the objective and terminates in finite time).

All imaging suffers from artifacts, errors introduced by the necessity of reconstructing images using incomplete models. Artifacts include Gibbs' ringing around edges, aliasing as a result of too-widely spaced samples, blurring, and various types of motion effects. Motion is a particular problem for cardiac

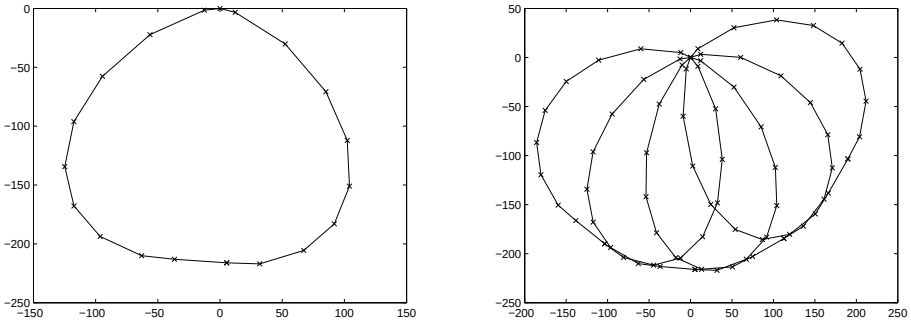

Figure 1. *Left:* One Teardrop trajectory in k-space. *Right:* Rotating one Teardrop trajectory around the centre of k-space.

imaging. One way of mitigating it is the use of velocity-insensitive control waveforms. Imposing velocity insensitivity results in dense constraints which are not amenable to fast heuristic methods, such as the original methods used in [1], and thus requires the more sophisticated optimization models and tools presented here.

MR imaging is controlled by different digital waveforms, subject only to loose physical constraints. This freedom is used to tune image acquisition protocols to each patient, including the positioning, resolution, and dimensions of individual imaged slices within the imaging volume. To give imaging technicians the most flexibility, this requires waveform optimization fast enough to match interactive manipulation of the imaging slice resolution and orientation, meaning subsecond solution times. Both models offer such times with commercial solvers which could be embedded in the software used by MR technicians.

The Teardrop gradient waveform is a continuous family of waveforms. It gets its name from the shape of the integrated waveform for short acquisition times, see figure 1.

We present two related models for designing Teardrop waveforms, which share the physical constraints designed to prevent device failure. They differ in how they constrain the maximum gap between neighbouring trajectories. The first model uses nonlinear constraints derived from the structure of Teardrop waveforms (symmetrical outward and inward spiral arms) and properties of the plane. The second algorithm involves solving a sequence of convex models with simpler (linear and quadratic) constraints. This could be exploited were a very fast solver (for larger problems) required. It does not use the fact that the waveforms describe interleaved spiral trajectories, only knowledge of which trajectories are neighbours. One of our motives in developing the second approach is to be able to optimize any waveform in two or three dimensions

when this adjacency information is available. The results of the two methods are equivalent, from the application point of view.

This paper is organized as follows: Section 2 reviews the required concepts in MR. The general methods of formulating optimization models of MRI Teardrop gradient waveforms and specifics for the nonlinear model are presented in section 3. This discussion includes: Teardrop waveform parametrization, the design objective, and constraints, including alternative formulations. The next section (4) modifies the general nonlinear constraints and objective for for the sequential SOC approach, and gives a proof of soundness. Section 5 details the implementation of the models, and computational results. Section 6 closes the paper with conclusions and recommendations for future work.

1.1 *Related work*

Accelerating MRI is an active research topic, with a long history going back to the introduction of echo-planar imaging (EPI), [4] in the early days of imaging. The fastest methods of reconstructing images follow EPI in spirit by sampling all or a substantial part of the data required to reconstruct an image continuously. Such data collection strategies include spiral, rosette, and Teardrop sampling.

A number of techniques have been put forth to design nulled moment gradient waveforms for motion compensation [5–11]. These are direct solution methods, with very limited constraints. They take advantage of the linear relationship between gradient waveform time moments and lobe amplitudes to generate motion compensated or sensitised waveforms. There are several potential deficiencies that may limit their effectiveness in gradient waveform design. Limitations on the incorporation of physical limits means that not all solutions are feasible. Refinements [9,12,13] iterate through algebraic solutions until feasible solutions are found. These methods do not guarantee that a feasible solution will be found even if one exists, nor do they produce optimal results.

Gradient waveform design has been described as a problem of nonlinear constrained optimization [9], and previous work has presented different methods of optimizing gradient waveforms in different situations [14–20]. But many of these methods are limited to the design of trapezoidal pulses, and most have been studied for one dimensional (1D) gradient design.

Hargreaves et al. [21] were the first to introduce optimized rewinders for the more difficult case of short spiral imaging. Rewinders, which are additional waveforms occuring after the normal spiral data collection, add overhead and take away from overall efficiency, unlike some of the methods for trapezoidal waveforms. This is why they only achieve a theoretical sampling duty cycle of 48 percent versus 78 for Teardrop.

2 MRI Basics

To understand the present design problem, we require the following facts from MR physics:

(i) the subject is in a large field, which imposes a preferred direction
(ii) protons precess around this field when not at equilibrium
(iii) the signals from all protons are measured by coils sensitive to the 'transverse' components, which can be combined into a complex-valued signal
(iv) localization of the signal is achieved indirectly using linear variations of field strength, which lead to linear variations in the precession of the magnetization and phase of the complex signal, which result in measurable interference
(v) the linear variations are controlled by *gradient coils* driven by amplifiers controlled by digital waveforms.

More detail is available in texts on MRI, including [22], [3].

2.1 *The k-Space and Basic 2D k-Space Patterns*

The key organizational concept in MR image reconstruction is k-space, see [23, 24], the dual space to physical space which parametrizes linear phase variations, also called spatial harmonics. Measured data is a sampling of the Fourier transform of the object density at individual points in k-space. In two-dimensional imaging, a thickened plane within the object is excited to produce a signal, and only gradients whose variation is tangent to that plane are used during data collection. The resulting signal s depends on the position in k-space

$$s(t) = \int_x \int_y m(x,y) e^{-i2\pi[k_x(t)x + k_y(t)y]} \, \mathrm{d}x\mathrm{d}y, \tag{1}$$

determined by integrating the gradient strengths G_x, G_y

$$k_x(t) = \frac{\gamma}{2\pi} \int_0^t G_x(\tau) \, \mathrm{d}\tau \tag{2}$$

$$k_y(t) = \frac{\gamma}{2\pi} \int_0^t G_y(\tau) \, \mathrm{d}\tau \tag{3}$$

called the position in k-space; $m(x,y)$ is the transverse nuclear magnetization, and γ is a physical constant relating the strength of a magnetic field to the

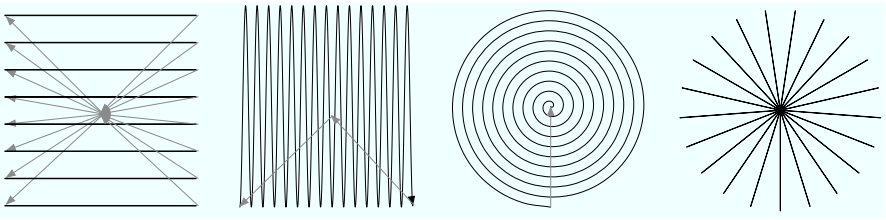

Figure 2. Raster, EPI, spiral and radial sampling patterns.

rate of precession. So

$$s(t) = \mathcal{M}(k_x, k_y), \tag{4}$$

where $\mathcal{M}$ is the 2D Fourier transform of $m(x, y)$, and k_x and k_y are given in units of spatial frequency, *e.g.* cycles/m.

To form an image, the trajectories given by $\{k(t)\}$ should cover a sufficient part of the k-space to allow reconstruction of $m(x, y)$. A variety of patterns have been developed for sampling and image reconstruction. The rectangular raster scan (figure 2 left) is used by standard two-dimensional Fourier transform (2DFT) imaging. Beginning at the origin, the k-space trajectory moves along the k_x direction as the signal is read out. A change in the amplitude of the G_y gradient leads to a different line in the k-space. By indexing to a set of k_y-positions, we can assemble sufficiently many measurements to fill the 2D k-space, and simply perform an inverse 2D Fourier transform to reconstruct the image. Undersampling with this trajectory produces recognizable aliasing artifacts called ghosts. Projection reconstruction imaging, sampling along radii or diameters, was (and is still) used because the resulting data can be reconstructed using low-complexity methods of inverting the Radon transform.

Spiral imaging samples along the locus of a spiral. The most common form of image reconstruction involves resampling the measurements onto a rectangular lattice and applying a fast Fourier transform.

The two most common artifacts particular to 2DFT images are the consequences of motion and undersampling, especially in the y direction. Undersampling means that not enough cycles are used in the data collection. This results in the samples not being sufficiently close in k-space and the bottom of the image appears to wrap around the top. This artifact is called aliasing. The cure is to increase the density of the samples.

In one dimension, with regular sampling, the Nyquist sampling theorem requires that inter-sample spacing, Δ_{k_x}, be bounded by the maximum repre-

sentable object size, the *field of view* (FOV),

$$\frac{1}{\Delta_{k_x}} \geq \text{FOV}. \tag{5}$$

This translates into a constraint on the spacing of lines in raster or radial sampling, and the spacing of spiral interleaves:

$$\Delta_{\text{inter-arm}} < \frac{1}{\text{FOV}}. \tag{6}$$

The effects of the subject's motion on the 2DFT image are complicated and multiple, but for very fast (subsecond) imaging the most important effect is caused by differences in the effect of gradient waveforms on static and dynamic tissues. The difference in phase for tissue at constant velocity is proportional to the first moment of the gradient waveforms, so we can put constraints on this moment [7]. Higher moments measure the effect of non-constant velocity (acceleration, change in acceleration, *etc.*), and can be incorporated by exactly the same methods we employ here for the first moment.

3 Nonlinear Optimization

To define an optimization problem, we must define

(i) variables (the discretized waveform),
(ii) an objective (maximize resolution), and
(iii) constraints (amplifier limits, aliasing, motion insensitivity).

3.1 *Teardrop Waveform Parametrization*

Since gradient waveforms are computer generated discrete functions and applied to the gradient coils via digital-to-analog (D/A) converters, the most obvious and general variable set is a discrete series of piecewise-constant gradient amplitudes. This set may be expressed in vector form as

$$\vec{g} = [g_1, g_2, \cdots, g_i, \cdots, g_{n+1}]^{\mathrm{T}} \in \mathcal{R}^{2n+2}, \tag{7}$$

where $g_i \in \mathcal{R}^2$ indicates the amplitude of the gradient waveform at time $t_i = i\triangle t$, and $\triangle t$ is the sample interval. The amplitudes at the $n+1$ points define the gradient waveform. Any gradient waveform shape can be expressed by such a gradient amplitude vector, thereby removing artificial constraints on

shape and expanding the feasible solution space to the limits of the gradient hardware system.

To present objective and constraints conveniently and efficiently in the Teardrop gradient waveform design, we add another variable set $\vec{k}$ which stands for a set of points in k-space.

$$\vec{k} = [k_1, k_2, \cdots, k_i, \cdots, k_n]^{\mathrm{T}} \in \mathcal{R}^{2n}, \text{ where} \tag{8}$$

$$k_i = \sum_{j=1}^{i} g_j \qquad i \in [1, \cdots, n]. \tag{9}$$

Note that there is one more point in the gradient amplitude space than in k-space in this formulation, but either set forms a complete set of variables and we will use the set which results in the clearest explanation, without comment.

3.2 *Objective: Maximize Resolution*

In k-space, low frequencies are near the centre of k-space, higher spatial frequencies are towards the edges. We know small structures and fine details of an image contain high spatial frequencies. So higher spatial frequencies give better spatial resolution. Thus, if we want a sharp image, we have to measure not only the low spatial frequencies but higher ones as well.

Our design goal is to maximize resolution. So our objective function can be expressed as

$$\max \begin{cases} ||k_{(n+1)/2}||_2 & n \text{ odd} \\ ||k_{n/2}||_2 + ||k_{n/2+1}||_2 & n \text{ even.} \end{cases} \tag{10}$$

This is not a convex function, so there are no guarantees we will reach a global minima.

3.3 *Constraints*

Gradient system hardware limitations, maximum interleaf spacing to prevent aliasing artifacts, and first moment nulling form the (hard) constraints for the design of Teardrop gradient waveforms.

3.3.1 *Gradient System Hardware Limitations.*

Amplitude Limits. Gradient amplifiers have peak current limits which restrict the maximum absolute value of gradient waveform amplitude. These limits can be expressed as inequality range constraints on each of the $n+1$ points in the discrete waveform sequence as

$$||g_i||_2 \leq G_{\max}, \quad i \in [1, n+1], \tag{11}$$

where $G_{\max}$ is the maximum allowable gradient amplitude.

Slew or Rise Time Limits. Gradient amplifiers also have limits on slew rate or rate of change of amplitude. This can be approximated as an inequality constraint on the first-order differences between adjacent points in the discretization as

$$||g_{i+1} - g_i||_2 \leq S_{\max}\Delta t, \quad i \in [1, \cdots, n+1], \tag{12}$$

where Δt is the duration of the sample interval.

3.3.2 ***Endpoint Constraints.*** Balanced SSFP acquisitions require zero starting and ending positions in k-space. The simplest approach is to start and end the readout at the centre of k-space, with no gradient activity:

$$g_1 = 0 \qquad k_1 = 0 \tag{13}$$

$$g_{n+1} = 0 \qquad k_n = 0. \tag{14}$$

(The exact form of the initial and final constraints may vary as a function of the design of the slice excitation, but these decisions are outside the scope of this paper, and do not change the character or structure of the problem.)

3.3.3 ***First Moment Nulling.*** In bSSFP imaging, we do not dephase (destroy by making incoherent) the magnetization from one readout to the next, but keep modifying it with new RF pulses. Since the magnetization is never reset, errors build up over time, which may magnify motion artifacts. To make the readout gradient motion-insensitive, we require the first moment to be zero:

$$\sum_{i=1}^{n+1} i g_i = 0. \tag{15}$$

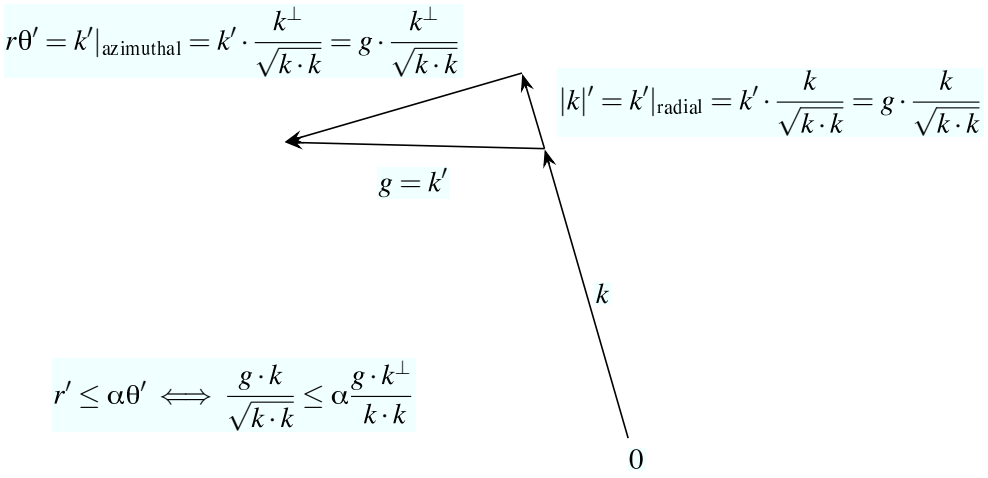

Figure 3. The deduction of the spiral constraint.

3.3.4 ***(Un)aliasing Constraint.*** Aliasing results if the separation between spiral interleaves is greater than 1/FOV. For a standard spiral in polar coordinates

$$r = \kappa\theta, \tag{16}$$

where r is the radial distance, θ is the polar angle, and κ is a constant. This constraint is satisfied if and only if $\kappa < 1/(2\pi\text{FOV})$. If r and θ are functions of time

$$r' \leq \kappa\theta'. \tag{17}$$

For an oppositely turning spiral, the constraint would be

$$-r' \leq \kappa\theta'. \tag{18}$$

We will use, without loss of generality, the two forms for the outward and inward halves of the Teardrop, respectively.

From figure 3, we know that the radial derivative r' at a point $k = (k_x, k_y)$ is $k \cdot g/||k||$ where $g = k'$ and $k \cdot g$ indicates the dot product of the vectors k and g. The angular derivative is $k^{\perp} \cdot g/||k||^2$, where $k^{\perp} = (-k_y,\ k_x)$ is the perpendicular vector of k. Substituting these in the constraint (17), we get

$$r' \leq \kappa\theta' \Leftrightarrow \frac{k \cdot g}{\sqrt{k \cdot k}} \leq \kappa \frac{k^{\perp} \cdot g}{k \ \cdot k}. \tag{19}$$

By squaring both sides of this formula, the constraint family can be written entirely in terms of polynomials as

$$(k_i \cdot g_i)(k_i \cdot g_i)(k_i \cdot k_i) \leq \kappa^2 (k_i^{\perp} \cdot g_i)(k_i^{\perp} \cdot g_i) \quad i \in [1, \cdots, n]. \tag{20}$$

3.4 *First Nonlinear Model*

Combining the objective and all the constraints together, we get the following optimization model when n is odd:

$$\begin{aligned}
\max \quad & ||k_{(n+1)/2}||_2 && \text{(21a)}\\
\text{subject to } & k_1 = 0 && \text{(21b)}\\
& k_n = 0 && \text{(21c)}\\
& g_1 = 0 && \text{(21d)}\\
& g_{n+1} = 0 && \text{(21e)}\\
& k_i = \sum_{j=1}^{i} g_j \quad i \in [1, \cdots, n] && \text{(21f)}\\
& ||g_i||_2 \leq G_{\max}, \quad i \in [1, \cdots, n+1] && \text{(21g)}\\
& ||g_{i+1} - g_i||_2 \leq S_{\max} \Delta t, \quad i \in [1, \cdots, n+1] && \text{(21h)}\\
& \sum_{i=1}^{n+1} i g_i = 0 && \text{(21i)}\\
& (k_i \cdot g_i)(k_i \cdot g_i)(k_i \cdot k_i) \leq \kappa^2 (k_i^{\perp} \cdot g_i)(k_i^{\perp} \cdot g_i) && \text{(21j)}\\
& \qquad i \in \{1, \cdots, \lfloor n/2 \rfloor - 1\},\\
& -(k_i \cdot g_i)(k_i \cdot g_i)(k_i \cdot k_i) \leq \kappa^2 (k_i^{\perp} \cdot g_i)(k_i^{\perp} \cdot g_i) && \text{(21k)}\\
& \qquad i \in [\lceil n/2 \rceil + 1, \cdots, n],
\end{aligned}$$

where n Δt is the sample interval, and κ is a constant.

When n is even, the objective becomes:

$$\max \quad ||k_{n/2}||_2 + ||k_{n/2+1}||_2 \tag{22}$$

while the constraints are the same.

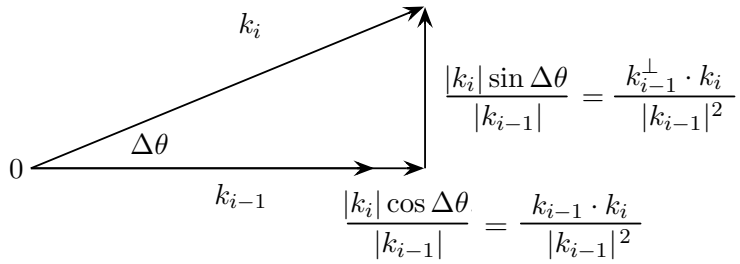

Figure 4. Diagram which leads to the trigonometric spiral constraint (25).

3.5 *Variation on the Nonlinear Model*

The most complicated constraint in the original model is the last one: the spiral constraint (21j)/(21k). By using the arctangent function, we can simplify this constraint significantly. From figure 4, we see

$$k_{i-1}^{\perp} \cdot k_i = |k_{i-1}||k_i| \cos(90^o - \Delta\theta) = |k_{i-1}||k_i| \sin \Delta\theta, \tag{23}$$

$$k_{i-1} \cdot k_i = |k_{i-1}||k_i| \cos \Delta\theta, \tag{24}$$

hence

$$\Delta\theta = \text{atan2}(k_{i-1}^{\perp} \cdot k_i,\, k_{i-1} \cdot k_i), \tag{25}$$

where $(x, y) \to (\sqrt{x^2 + y^2}, \text{atan2}(y, x))$ is the transformation from Cartesian to polar coordinates. The two-argument arctangent distinguishes opposite directions, which the single-argument version does not.

Integrating $r \leq \kappa\theta$ gives an approximation $\Delta r \leq \kappa\Delta\theta$ which is satisfied if and only if

$$||k_i||_2 - ||k_{i-1}||_2 \leq \kappa \, \text{atan2}(k_{i-1}^{\perp} \cdot k_i, k_{i-1} \cdot k_i), \quad i \in \{1, \ldots, \lfloor n/2 \rfloor\}, \tag{26}$$

which is an alternative to constraint (21j). Reversing the sign gives the alternative to (21k).

The alternative spiral constraints (26) are still nonlinear and nonconvex, and not applicable to general trajectory shapes, including three-dimensional trajectories. They depend on the discrete rotational symmetry, which interchanges any two trajectories, and the cycle of adjacency relationships.

4 Sequential Convex Optimization

In this section we define a general approach which works with any set of adjacency relationships, with or without symmetry. We define a sequence of problems, $\{P_i\}$, where P_i is defined in terms of the solution to P_{i-1}, and each subproblem is convex with only linear and SOC constraints. To do so we must transform the nonconvex constraints (26) into convex constraints, and make the objective linear.

4.1 *(Un)aliasing constraints*

To generalise the spiral constraint we need to add another set of points in k-space as variables:

$$\vec{k''} = [k''_1, k''_2, \cdots, k''_i, \cdots, k''_n]^{\mathrm{T}} \in \mathcal{R}^{2n}. \tag{27}$$

We impose the rotational relationship with additional constraints

$$k''_i = \begin{pmatrix} \cos\phi & \sin\phi \\ -\sin\phi & \cos\phi \end{pmatrix} k_i, \tag{28}$$

where $\phi = 2\pi/(\text{the number of interleaves})$. The spiral constraint can now be replaced by a general proximity constraint:

$$\min_j \beta_{i,j} \leq \frac{1}{\mathrm{FOV}}, \quad \forall i \in \{1, ..., n\}, \tag{29}$$

where

$$\beta_{i,j} = \mathrm{distance}(k''_i, \overline{k_j k_{j+1}}) \tag{30}$$

is the distance between a control point on the second trajectory and a line segment of the first trajectory. Referring to figure 5, $\beta_{i,j}$ can be calculated as

$$\beta_{i,j} = \min_{\alpha \in [0,1]} ||\alpha\, k_{j+1} + (1-\alpha)\, k_j - k''_i||_2. \tag{31}$$

To define the new constraint concretely in terms of the old solution, we use the fact that the minimum occurs at

$$\alpha_{i,j} = \begin{cases} \widetilde{\alpha} & \text{if } 0 < \widetilde{\alpha} < 1 \\ 1 & \text{if } \widetilde{\alpha} \geq 1 \\ 0 & \text{if } \widetilde{\alpha} \leq 0 \end{cases}, \text{ where} \tag{32}$$

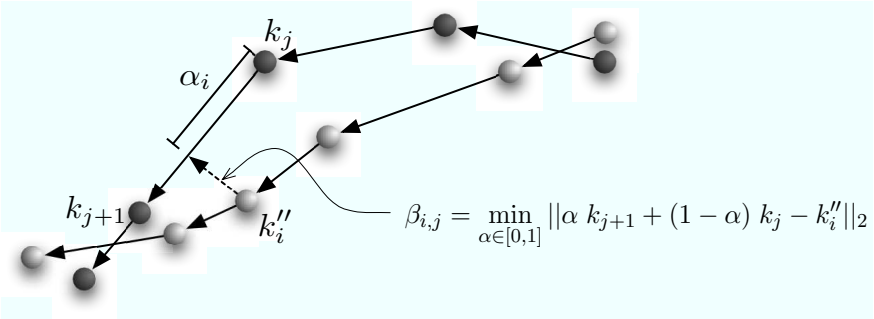

Figure 5. Limit the distances between two trajectories.

$$\widetilde{\alpha} = \frac{(k''_{i,\text{old}} - k_{j,\text{old}}) \cdot (k_{j+1,\text{old}} - k_{j,\text{old}})}{||k_{j+1,\text{old}} - k_{j,\text{old}}||^2}. \tag{33}$$

Letting,

$$\gamma_i = \text{argmin}_j\, \beta_{i,j}, \tag{34}$$

the new constraint is

$$||\alpha_{i,\gamma i}\ k_{\gamma i+1} + (1-\alpha_{i,\gamma i})\ k_{\gamma i} - k_i''||_2 \leq \frac{1}{\text{FOV}}, \tag{35}$$

which says that the point on the adjacent trajectory closest to a point in the old solution is now constrained to lie within the Nyquist sampling distance of the corresponding point in the new solution. Since γ_i and $\alpha_{i,j}$ depend on the previous solution and on variables in the current problem, the constraint is convex quadratic.

4.2 *Linear objective*

We replace the old objective function by

$$\max \begin{cases} k_{N+1} \cdot \bar{k}, & n = 2N+1 \\ (k_N + k_{N+1}) \cdot \bar{k}, & n = 2N \end{cases} \tag{36}$$

where

$$\bar{k} = \begin{cases} k_{N,\text{old}}/|k_{N,\text{old}}|, & n = 2N+1 \\ \frac{(k_{N,\text{old}}+k_{N+1,\text{old}})}{|k_{N,\text{old}}+k_{N+1,\text{old}}|}, & n = 2N \end{cases}. \tag{37}$$

The new objective seeks to expand the trajectory in k-space in the same direction as the maximal point of the previous solution.

4.3 *Symmetry reduction*

We now show how to use the problem symmetry to cut the number of variables in the problem in half, which for brevity we will only do for the case $n = 2N+1$. In this case k_N is the middle point of the Teardrop trajectory. In our new model, we only need to optimize $N+1$ points (the first half of the trajectory), reproducing the other half by reflection.

Most of the constraints come in families with each constraint involving only one or two adjacent points. Symmetry reduction for these constraints involves dropping constraints on dropped points. Expressing the first moment nulling constraint (21i), however, can only be done in combination with the condition $k_n = 0$, which says that the zeroth moment is zero. Using the direction of the middle point of the previous iteration $\bar{k}$, and its perpendicular vector $\bar{k}^{\perp}$, as defined above, the trajectory is symmetric precisely when

$$g_{i+N+1} \cdot \bar{k} = -g_{N+2-i} \cdot \bar{k}, \text{ and} \tag{38}$$

$$g_{i+N+1} \cdot \bar{k}^{\perp} = g_{N+2-i} \cdot \bar{k}^{\perp}. \tag{39}$$

To satisfy the constraint (21i), it is necessary and sufficient to satisfy the following equalities:

$$\bar{k} \cdot (\sum_{i=1}^{2N+2} i g_i) = 0, \tag{40}$$

$$\bar{k}^{\perp} \cdot (\sum_{i=1}^{2N+2} i g_i) = 0. \tag{41}$$

Using (21f) to add (21c) in the equivalent form $\sum g_i = 0$ to (21i) we obtain (40):

$$\begin{aligned} \bar{k} \cdot (\sum_{i=1}^{2N+2} (i+1/2) g_i) &= \textstyle\sum_{i=1}^{2N+2} (i+1/2) g_i \cdot \bar{k} \\ &= \textstyle\sum_{i=1}^{N+1} (i+1/2) g_i \cdot \bar{k} + \sum_{i=N+2}^{2N+2} (i+1/2) g_i \cdot \bar{k} \\ &= \textstyle\sum_{i=1}^{N+1} (i+1/2) g_i \cdot \bar{k} + \sum_{j=1}^{N+1} (N+3/2+j) g_{N+1+j} \cdot \bar{k} \\ &= \textstyle\sum_{i=1}^{N+1} (i+1/2) g_i \cdot \bar{k} + \sum_{\tilde{j}=1}^{N+1} (\tilde{j}+1/2)(-g_{\tilde{j}}) \cdot \bar{k} \\ &= 0. \end{aligned} \tag{42}$$

Similarly,

$$\bar{k}^{\perp}\cdot(\sum_{i=1}^{2N+2} ig_i) = \sum_{i=1}^{N+1}(i+1/2)g_i\cdot\bar{k}^{\perp}+\sum_{j=1}^{N+1}(j+1/2)(g_{j+1/2}\cdot\bar{k}^{\perp} = 2\bar{k}^{\perp}\cdot\sum_{i=1}^{N+1}(i+1/2)g_i. \tag{43}$$

So we have one real constraint (instead of four) after doing a symmetry reduction.

4.4 *Subproblem*

Keeping all other constraints the same as before, we obtain the following convex model for the subproblem:

$$\begin{aligned}
\max \quad & k_N \cdot \bar{k} && \text{(44a)}\\
\text{subject to} \quad & k_1 = 0 && \text{(44b)}\\
& g_1 = 0 && \text{(44c)}\\
& k_i = \sum_{j=1}^{i} g_j, \quad i \in [1, N+1] && \text{(44d)}\\
& ||g_i||_2 \le G_{\max}, \quad i \in [1, N+1] && \text{(44e)}\\
& ||g_{i+1} - g_i||_2 \le S_{\max}\Delta t, \quad i \in [1, N] && \text{(44f)}\\
& \sum_{i=1}^{N+1}(i+1/2)g_i = 0 && \text{(44g)}\\
& k_i'' = \begin{pmatrix} \cos\phi & \sin\phi \\ -\sin\phi & \cos\phi \end{pmatrix} k_i, \quad i \in [1, N] && \text{(44h)}\\
& ||\alpha_{i,\gamma_i}\cdot k_{\gamma_i+1} + (1-\alpha_{i,\gamma_i})\, k_{\gamma_i} - k_i''||_2 \le d, && \text{(44i)}\\
& \quad i \in [2, N],
\end{aligned}$$

where Δt is the sample interval, γ_i and α_{i,γ_i} are chosen according to (34) and (32), $\bar{k} = k_{N,\text{old}}/|k_{N,\text{old}}|$, and d is a constant usually chosen to be 1/FOV.

4.5 *Iteration*

To solve the nonlinear problem, we start with a spiral: given by

$$k_i = c_0(\cos(c_1 i), \sin(c_1 i)),$$

Input:
initial values $k_{i,\text{old}},\ k''_{i,\text{old}} \quad i \in [1,n]$;
tolerance: a parameter which stands for the tolerance of the objective function.
begin
iter := 1;
previous-obj := 0;
$k_i := k_{i,\text{old}},\ k''_i := k''_{i,\text{old}} \quad i \in [1,\cdots,n]$;
calculate α_i by using Formula (32);
solve;
repeat
{
$k_i := k_{i,\text{old}},\ k''_i := k''_{i,\text{old}} \quad i \in [1,\cdots,n]$;
recalculate α_i by using Formula (32);
previous-obj := current-obj;
solve the optimization problem (44);
$i := i+1$;
} until current-obj <= previous-obj + tolerance.
end.
end.

Figure 6. The pseudocode of the iterative nonlinear method.

and alternately define a convex problem (44), and then solve that problem, until we fail to achieve a sufficient increase in resolution. See figure 6 for a pseudocode description.

4.6 *Convergence*

We cannot hope to guarantee that the result of the iterative algorithm (figure 6) is a global optimal solution because the original model is not convex. What we will prove is that the top-level objective value, the maximum resolution (radius in k-space), increases monotonically (with each iteration) to a limit. This means the sequential approach is worth doing (it improves resolution) and using failure to produce a sufficient increase in resolution as a stopping criteria will result in a finite number of iterations. It doesn't say we will reach a local maximum, something we haven't even defined for the sequential approach, although we clearly hope it will converge to a local maximum of the nonlinear problem. In many experiments, the nonlinear and sequential methods found the same solutions.

LEMMA 4.1 *The union of the feasible sets of all subproblems* (44) *has compact closure.*

Proof The common constraints (11) define a compact set containing the feasible set for all subproblems. □

LEMMA 4.2 *The previous solution, k_{old}, is a feasible point for the subproblem* (44) *it defines.*

Proof All subproblems share constraints (44b)-(44h), so they are satisfied by k_{old}. The previous solution k_{old} satisfies the proximity constraint (44i) for the old values of α and γ. Since the new values defined by (32) and (34) minimize the norm (by definition), we have

$$\begin{aligned}&\left\|\alpha_{i,\gamma_i} k''_{\gamma i,\text{old}} + (1-\alpha_{i,\gamma_i}) k''_{\gamma i,\text{old}} - k_{i,\text{old}}\right\| \\ &\qquad \leq \left\|\alpha_{i,\gamma_{i,\text{old}},\text{old}} k''_{\gamma i,\text{old,old}} + (1-\alpha_{i,\gamma_{i,\text{old}},\text{old}}) k''_{\gamma i,\text{old}} - k_{i,\text{old}}\right\| \leq d. \quad (45)\end{aligned}$$

So k_{old} satisfies (44i) and hence is a feasible point for the new problem. □

Practically, this allow us to use a feasible interior point method to solve the subproblems.

LEMMA 4.3 *The solution, k, of the subproblem* (44) *constructed from k_{old} satisfies*

$$\|k_N\| \geq \|k_{N,old}\| .$$

Proof The starting point has objective $k_{N,\text{old}} \cdot \bar{k} = \|k_{N,\text{old}}\|$ by the definition of $\bar{k}$ following (44). The objective at the optimum cannot be smaller, since the old solution is a feasible point for the new problem, by the previous lemma. It follows from the triangle inequality that

$$\|k_N\| = \|k_N\| \left\|\bar{k}\right\| \geq \left\|k_N \cdot \bar{k}\right\| \geq \left\|k_{N,\text{old}} \cdot \bar{k}\right\| = \|k_{N,\text{old}}\| \left\|\bar{k}\right\| = \|k_{N,\text{old}}\| .$$

□

LEMMA 4.4 *The sequence given by solving subproblems successively formed from previous solutions has converging objective values.*

Proof The norm $\|k_N\|$ is a continuous function on a compact set and hence bounded. The sequence of $\{\|k_N\|\}$ is increasing, so it must converge to a limit point. □

In practice, the subproblems converge rapidly, not only in the objective, but uniformly in all variables, even though the four lemmas do not rule out

non-singleton limit sets. For example, the reflection

$$k_i \mapsto 2(\bar{k} \cdot k_i)\bar{k} - k_i$$

is a symmetry on the set of limit points. We conjecture that convergence in all variables is a result of using previous solutions as starting points for the subproblems they define, but for practical purposes, only convergence in the objective matters.

5 Implementation and results

We implemented the algorithm in the modelling environment AMPL. The AMPL language contains all the features required to define optimization problems, including bi-level and iterative problems using a `repeat` construction. The main advantages of the AMPL environment is the ability to evaluate different solvers on the same optimization problem and to make model changes quickly. Both LOQO [25] and IPOPT [26] solve the nonlinear model in a couple of seconds.

For the iterative method, several more solvers are available. We used MOSEK [27] because it had excellent performance, although solution times for Teardrop are fast enough that any solver capable of handling SOC constraints should be able to handle it. We also tried solving larger models for three-dimensional generalisations of Teardrop (as detailed in [28], including AMPL code for both the two-dimensional Teardrop and three-dimensional problems), but found the development very difficult as a result of the lack of integrated visualization. In another paper, [29], we will describe software integrating visualization with the solver and a heuristic approach to designing trajectories in three dimensions also based on SOC constraints, but without proximity constraints. Using the integrated environment, we plan to apply the ideas developed here for proximity constraints to the new approach.

5.1 *Computational Results*

In this section we present the computational results of the Teardrop2D.mod model solved by MOSEK [27]. The MOSEK optimization software is designed to solve large scale mathematical optimization problems. It can solve linear, convex quadratic and general convex mathematical programs. An interior point optimizer is available for all supported problem classes. All numerical experiments were performed on an IBM RS/6000 44P Model 270 workstation, with 8 GB memory and 375 MHz processor.

Figure 7 presents the k-space trajectories obtained by iteratively solving the

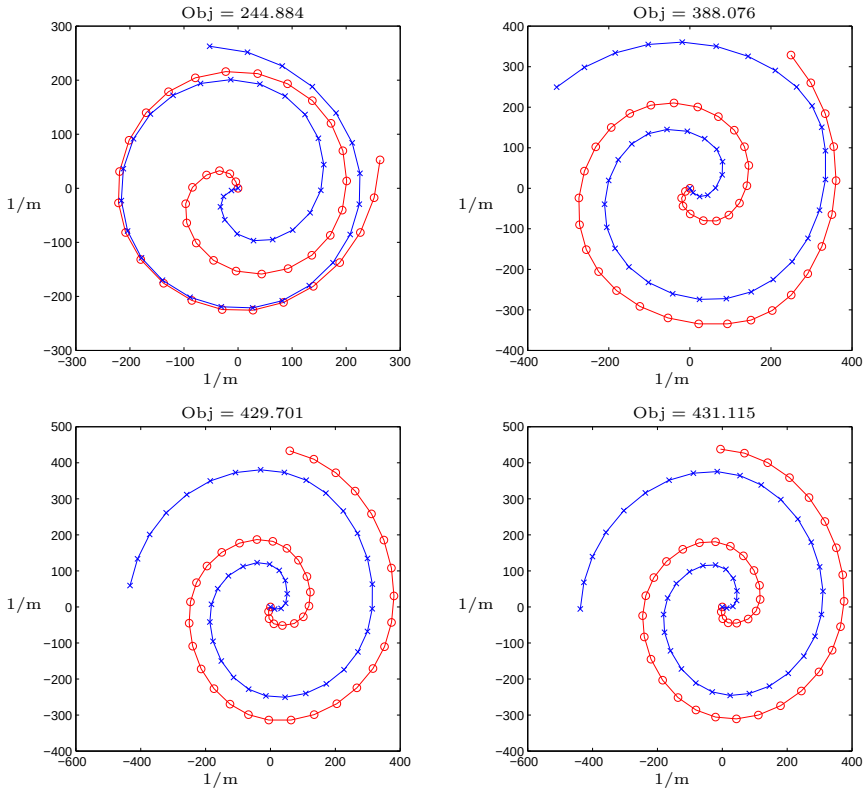

Figure 7. Teardrop trajectories after iterations 1, 4, 8 and 10, the last iteration.

subproblems without the first moment nulling constraint. After ten iterations, we obtained the optimal result. From these figures, we can see the objective function value is increasing from iteration to iteration. In the meantime, the trajectories are becoming more and more evenly spaced as expected.

Figure 8 presents the the optimal trajectories obtained by iteratively solving the subproblems (44) (with first moment nulling) twelve times. Comparing this result to the result without first moment nulling (figure 7), we note a small decrease in the top-level objective.

The k-space trajectories we obtained from the model have been reduced using symmetry reduction. We use that symmetry to recover the full trajectories. For example, figure 9 (left) shows one full Teardrop trajectory corresponding to the half trajectory in figure 7. Rotating the associated gradient profiles is equivalent to rotating the trajectory around the centre of k-space. Together the combined views cover the two-dimensional k-space completely, as seen on the right side of the same figure.

Figure 10 presents the corresponding optimal gradient waveforms in the

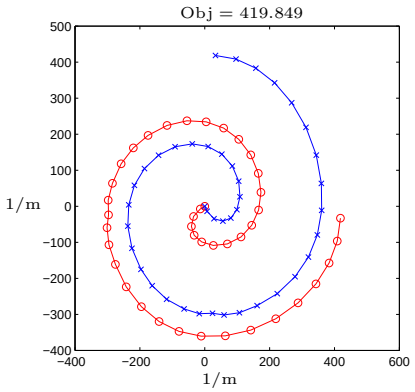

Figure 8. Teardrop trajectories with first moment nulling.

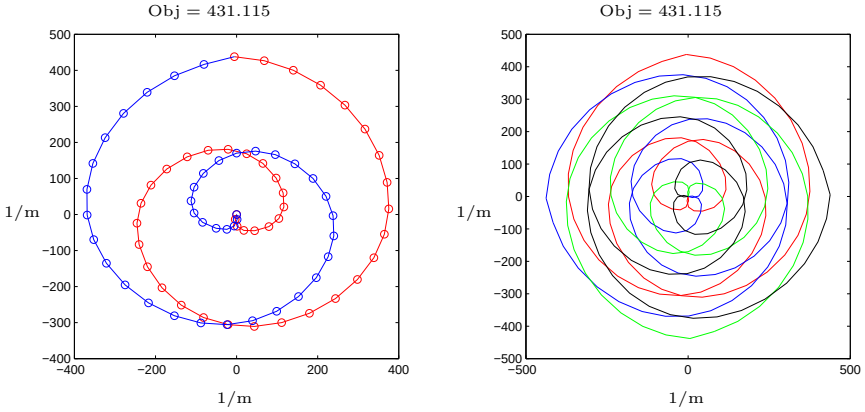

Figure 9. *Left:* One optimal Teardrop trajectory. *Right:* Four interleaved Teardrop trajectories.

x- and y-direction which generate one of the final trajectories of figure 7. Waveforms for the other interleaves are linear combinations of these two.

6 Conclusions and Future Work

We have demonstrated two approaches to designing resolution maximizing Teardrop waveforms, incorporating motion insensitivity for the first time in a readout waveform of this complexity. The approach using general nonlinear optimization involves constraints specific to waveforms incorporating interleaved spiral arms. The sequential approach uses convex subproblems which can be solved by several commercial and open-source solvers, and the proximity constraints apply to any trajectory design problem in which pairs of

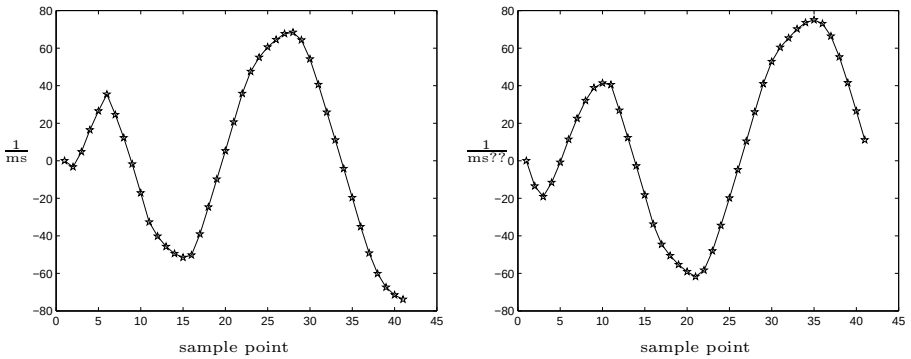

Figure 10. Gradient waveforms G_x and G_y for the 2D k-space.

adjacent trajectories are known. Although we cannot prove the sequential approach produces a local minimum, we have shown it is a sound algorithm and, in numerous tests, it closely matches solutions of the nonlinear problem.

We will happily provide both waveforms and the AMPL models to design them to other researchers, and hope that Teardrop will be applied to various types of imaging. Our current research focus is to incorporate the ideas developed here for the sequential model into three-dimensional design problems.

7 Acknowledgements

We would like to thank NSERC, CFI, OIT, and MITACS for financial support.

References

[1] Anand, C.K., Thompson, M., Wu, D.H. and Cull, T, 2001, Teardrop, a novel non-raster readout for true FISP. *ISMRM*, **9**, 1804.

[2] Nayak, K.S. and Hu., B.S., 2005, The Future of Real-time Cardiac Magnetic Resonance Imaging. *Current Cardiology Reports*, **7**, 45-51.

[3] Haacke, E.M., Brown, R.W., Thompson, M.R. and Venkatesan, R., 1999, *Magnetic Resonance Imaging: Physical Principles and Sequence Design*. (Toronto: John Wiley and Sons).

[4] Mansfield, P., 1977, Multi-planar image formation using NMR spin echoes. *J Phys C*, **10**, L55-L58.

[5] Haacke, E.M. and Lenz, G.W., 1987, Improving MR image quality in the presence of motion by using rephasing gradients. *American Journal Roentgenology*, **148**, 1251-1258.

[6] Keller, P.J. and Wehrli, F.W., 1988, Gradient moment nulling through the N-th moment. Application of Binomial Expansion Coefficients to Gradient Amplitudes. *Journal of Magnetic Resonance*, **78**, 145-149.

[7] Pattany, P.M., Phillips, J.J., Chiu, L.C., Lipcamon, J.D., Duerk, J.L., McNally, J.M. and Mohapatra, S.N., 1987, Motion artifact suppression technique (MAST) for MR imaging. *Journal of Computer Assisted Tomogrraphy*, **11**(3), 369-377.

[8] Pipe, J.G. and Chenevert, T.L., 1991, A progressive gradient moment nulling design technique. *Magnetic Resonance in Medicine*, **19**, 175-179.

[9] Wendt, R.E. III, 1991, Interactive design of motion compensated gradient waveforms with a personal computer spreadsheet program. *Journal of Magnetic Resonance*, **1**, 87-92.
[10] Xiang, Q.S. and Nalcioglu, O., 1987, A formalism for generating multiparametric encoding gradients in NMR tomography. *IEEE Transactions on Medical Imaging*, **MI-6**(1), 14-20.
[11] Yamagata, H., Bounocore, M.H., Telford, B. and Sanders, J.A., 1989, Optimized gradient pulses for MR quantitative flow imaging. *Radiology*, **173**(P), 162.
[12] Duerk, J.L., 1986, Magnetic resonance imaging gradient modulation technique for motion artifact reduction and flow quantification. Ph.D. Thesis, Dept. Biomed. Eng., Case Western Reserve University, Cleveland, OH.
[13] Groen, J.P., van Dijk, P. and In den Kleef, J.J.E., 1987, Design of flow adjustable gradient waveforms. *Book of Abstracts*, Soc. Magnetic Resonance in Medicine, Sixth Annual Meeting, p. 868.
[14] Atalar, E. and McVeigh, E.R., 1994, Minimizing dead-periods in MRI pulse sequences for imaging oblique planes. *Magn. Reson. Med.*, **32**, 773-777.
[15] Bolster, B.D. and Atalar, E. Jr., 1999, Minimizing dead-periods in flow-encoded or compensated pulse sequences while imaging in oblique planes. *J. Magn. Reson. Imaging*, **10**, 183-192.
[16] Dale, B.M. and Duerk, J.L., 2002, Time-optimal control of gradients. *Proceedings of the 10th Annual Meeting of ISMRM, Honolulu*, p. 2361.
[17] Heid, O., 2002, The fastest circular k-space trajectories. In: *Proceedings of the 10th Annual Meeting of ISMRM*, Honolulu, p. 2364.
[18] Morgan, V.L., Price, R.R. and Lorenz, C.H., 1996, Application of linear optimization techniques to MRI phase contrast blood flow measurements. *Magnetic Resonance Imaging*, **14**, 1043-1051.
[19] Simonetti, O.P., Duerk, J.L. and Chankong, V., 1993, An optimal design method for magnetic resonance imaging gradient waveforms. *IEEE Transactions on Medical Imaging*, **12**, 350-360.
[20] Simonetti, O.P., Duerk, J.L. and Chankong, V., 1993 MRI gradient waveform design by numerical optimization. *Magnetic Resonance in Medicine*, **29**, 498-504.
[21] Hargreaves, B.A., Nishimura, D.G. and Conolly, S.M., 2004, Time-optimal multidimensional gradient waveform design for rapid imaging. *Magnet Resonance in Medicine*, **51**, 81-92.
[22] Nishimura, D.G., 1996, *Principles of Magnetic Resonance Imaging*. Dept. of Electrical Engineering, Stanford University, CA.
[23] Ljunggren, S., 1983, A simple graphical representation of fourier-based imaging methods. *Journal of Magnetic Resonance*, **54**, 338-343.
[24] Twieg, D.B., 1983, The k-trajectory formulation of the NMR imaging process with applications in analysis and synthesis of imaging methods. *Medical Physics*, **10**, 610-621.
[25] Vanderbei, R.J., 1999, LOQO: An interior point code for quadratic programming. Optimization Methods and Software, **12**, 451484.
[26] Wächter, A. and Biegler, L. T., 2006, On the Implementation of a Primal-Dual Interior Point Filter Line Search Algorithm for Large-Scale Nonlinear Programming, *Mathematical Programming* **106**(1), 25-57.
[27] Fourer, R., Gay, D.M. and Kernighan, B.W., 1993 *AMPL: A Modeling Language For Mathematical Programming*. The Scientific Press.
[28] Ren, T., 2005, An Optimal Design Method for MRI Teardrop Gradient Waveforms. MSc thesis, McMaster University, Hamilton, ON.
[29] Anand, C.K., Curtis, A.T. and Kumar, R., Durga: A heuristically-optimized data collection strategy for volumetric magnetic resonance imaging. Preprint.